An Investigation of Synthesis, Electrochemistry and Thermal Stability of Ball-milled Si-based Alloy Anodes in Lithium-ion Batteries

Zhang Xingyu[1, ^], Wang Luqi[3, ^], Zheng Tianye[1], Lam Kwok-ho[1,2 *]

[1]Department of Electrical Engineering, The Hong Kong Polytechnic University, Hung Hom, Kowloon, Hong Kong

[2]Centre for Medical and Industrial Ultrasonics, James Watt School of Engineering, University of Glasgow, Glasgow, Scotland, United Kingdom

[3]Faculty of Science and Engineering, The University of Manchester, Oxford Rd, Manchester, M13 9PL, England, United Kingdom

*Corresponding author. Email: kokokh.lam@polyu.edu.hk.

kwokho.lam@glasgow.ac.uk

^Equal contributor

Abstract

The huge volume change of Si anode with fast capacity degradation limits its commercialization in LIBs. The co-introduction of metal and O elements into the Si bulk fabricating Si-metal silicide-Si oxides composites has been proven an effective way to overcome this issue. Among them, Si-CuO composites, due to financial feasibility and environmentally compatibility, have attracted much attention recent years but still with the unsatisfactory cycle performance. In order to optimize the cycle stability of Si-CuO composites, NiO is firstly introduced into the Si-CuO system with different proportion from 10 % to 20 % by a facile and low-cost HEBM method. The study reveals that $Si_{72}CuO_8NiO_{20}$, with the least volume change percentage of ~ 133 %, has a highest capacity retention of ~ 86. 9% after 100 cycles at 0.2 C and average coulombic efficiency of ~ 99.4 % as well as a competitive

volumetric capacity of ~ 1700 $Ah \cdot L^{-1}$ based on the 2nd lithiation. These results confirm the effectiveness of the NiO introduction to improve the cycle performance of the Si-CuO composites. Moreover, in order to make sure the ball-milled Si-CuO-NiO precursors can be well compatible with the high-temperature post-treatment of coating a carbon layer, the thermal stability of $Si_{72}CuO_8NiO_{20}$ is also conducted with the best cycle stability at 600 °C.

Introduction

The conventional graphite anode in Li-ion batteries (LIBs) has not yet met the market demand due to its relatively low capacity, ~ 370 $mAh \cdot g^{-1}$ or ~ 719 $Ah \cdot L^{-1}$ [1, 2]. Compared with graphite, silicon (Si) has a higher specific capacity of ~ 3580 $mAh \cdot g^{-1}$ or ~ 2194 $Ah \cdot L^{-1}$ at the room temperature, corresponding to an about 34% increase in energy density of a full cell, even when application standards are considered [2, 3]. This makes Si one of the most promising anodes for the next generation LIBs. However, one of the biggest challenges faced by Si anodes is the fast capacity fading caused by the huge volume changes during the lithiation-delithiation processes [2]. To be specific, Li insertion could increase the volume of Si by ~ 280% while Li extraction would in principle cause a lattice shrinkage by the same degree [2]. Such repetitive volume expansion and contraction during cycling would lead to the disruption of Si particles and unstable solid electrolyte interphase (SEI), resulting in the poor electrical contact between active materials and conductive matrix, mechanical failure of the electrode, and a higher impedance in the cell [4-6]. Accordingly, more Li^+ will likely be trapped in the bulk of Si during the delithiation process and simultaneously some Li^+ are irreversibly consumed due to the secondary

SEI formation [7]. Therefore, it is the key to alleviate the large volume change of Si anode for achieving the ideal electrochemical performance.

Applying transition metal elements (M) to alloy with Si and form Si/metal silicides can be an effective way to mitigate the aforementioned issues. The formed metal silicides are generally inactive to Li^+ [8] or have limited lithiation capacities [9, 10]. When Si particles are dispersed in the inactive matrix, its volume change can be effectively diluted [11, 12]. Although with sacrifice of some gravimetric specific capacity, the resulted volumetric specific capacity and energy density in Si-M alloy anodes are still quite competitive [13]. Practically, the high-energy ball-milling (HEBM) is an efficient method for synthesizing Si-M alloys anodes. During the milling process, the nanocrystalline Si with a high amorphous degree can be obtained, which is also considered a positive effect on the cycle performance [14, 15]. Based on the above advantages, there are already extensive works focusing on fabricating Si-M alloy anodes via HEBM method these years, like Si-Mo [16], Si-W [17], Si-Mn [18], Si-Ti [19], Si-Ni [20], Si-Fe [8], and Si-Cu [21] systems. These investigations indicate the enormous application potential of ball-milled Si-M alloy anodes, and the better electrochemical performance is still desirable for commercialization [22].

The recent studies revealed the introduction of O element into Si-M alloy anodes can further improve the cycle performance and coulombic efficiency and such Si-based anodes mainly consist of Si, doped metal silicides and amorphous Si oxides [22, 23]. In addition to maintain the merit of silicide, amorphous Si oxides can also be intercalated by Li^+ producing inactive lithium silicates in the first cycle [22], which are significantly helpful to buffer the large volume change of Si yielding a more stable SEI and longer life cycle [24]. Nevertheless, the formation of Si oxides is usually conducted under the high-temperature condition (approximately 1400 °C) via the

reaction between Si and SiO_2, which is an energy-consuming and expensive process [25-27]. Therefore, a low-cost and facile method for O introduction into Si-M systems would be necessary. Considering the suitability of HEBM method for fabricating Si-M alloy anodes and large-scale production, a feasible solution is to use a metal oxide substituting for a pure metal element to alloy with Si. Under the condition of non-equilibrium driven by high mechanical energy [28], the processed Si-based composites are expected to produce metal silicides and amorphous Si oxides simultaneously. This HEBM approach has been evaluated recently by Chia-Chin Chang's group [28, 29] and Peng Yu's group [30]. Both groups used Si and CuO as the raw materials to synthesize the Si-CuO composites. With the synergistic effect of the in-situ generated Cu_3Si and Si oxides, the ball-milled Si-CuO composites yielded enhanced cycle stabilities. Moreover, the fabrication of Si-CuO composites is claimed to be financial/technical feasible and environmentally compatible, showing great promises in enabling high energy Si-based anodes [9]. Yet there is still much room for improvement of ball-milled Si-CuO composites, and therefore investigations and optimizations are favored.

Herein, we firstly propose an alternative way of introducing NiO to the ball-milled Si-CuO composites to optimize the electrochemical performance. The reasons choosing NiO are as following: 1) the introduction of NiO could also provide O element to the Si-based composites forming more Si oxides. Simultaneously, NiO is predicted to react with Si to form $NiSi_2$ within a proper ratio range [20]; 2) Different from Cu_3Si, $NiSi_2$ is a Si-rich compound meaning there will be more active Si stored in the metal silicide when part of CuO is replaced with NiO. Correspondingly, the volume change of Si-based anodes would be effectively diluted [12]; 3) The ball-milled Si-based precursors often need to a post-treatment of coating a protective

carbon layer for further enhancing the electrical conductivity, alleviating the volume change, stabilizing the SEI and prolonging life cycle [17, 28, 31]. However, this post-treatment is generally a high-temperature process [22] and a high-quality carbon coating requires ball-milled Si-based precursors to maintain the nano-crystalline/amorphous microstructure as much as possible [5, 16]. Due to a higher melting point of Ni (~ 1453 ℃) than the one of Cu (~ 1083.4 ℃), the introduction of NiO would be expected to impart good high-temperature tolerance onto the composites [16, 17]. Therefore, we present the HEBM-synthesized of Si-CuO-NiO composites in a systematic way and compare them with Si-CuO composites. The influences of introducing NiO into the Si-CuO system on the electrochemistry behavior and the cycle performance are highlighted. In addition, a post high-temperature annealing process was also evaluated regarding the cycle stability of the specific Si-CuO-NiO composite.

Experimental

Synthesis of Si-CuO/Si-CuO-NiO samples. The samples were synthesized by the high-energy ball-milling machine (Model HCX-YY-TC-2L, Kunming Haichuangxing Technology Co. Ltd. Yunnan, China) . The mass ratio of ZrO_2 balls (ø = 3 mm; 2 kg) to the Si-based powders (90 g) was 20:1 and the rotation speed was set at 1200 rpm. To start with, we introduced a protective gas (Ar) into the milling chamber. The total milling time was 4 h, during which ~0.5 g powder samples were taken out per hour to undergo the X-ray diffraction (XRD) test. For all Si-CuO-NiO samples, the mass ratio of Si powder (the mean particle size is ~ 4 μm, Zhejiang Lichen New Materials Technology Co. Ltd, China) to CuO (99.5%, 100 – 200 nm, Macklin) is fixed at 9:1. Then, the mass percentage of NiO (99.0%, -325 mesh,

Aladdin) addition was adjusted to cover the range from 10% to 20%, referring to $Si_{81}CuO_9NiO_{10}$, $Si_{76.5}CuO_{8.5}NiO_{15}$ and $Si_{72}CuO_8NiO_{20}$. For comparison reasons, $Si_{90}CuO_{10}$ and $Si_{76.5}CuO_{23.5}$ were also prepared and tested to represent 0% NiO samples. Lastly, $Si_{72}CuO_8NiO_{20}$ was chosen for the assessment of high-temperature tolerance sintered at 600, 800 and 900 ℃ for 3 h in the Ar atmosphere, referring to $Si_{72}CuO_8NiO_{20}$-600, $Si_{72}CuO_8NiO_{20}$-800 and $Si_{72}CuO_8NiO_{20}$-900, respectively.

Material Characterizations

The phase structures of the samples were determined by a Panalytical desktop Aeris X-ray diffraction (XRD, Cu Kα) equipment from 10° to 80° with a scanning rate of 5°/min. Surface morphologies of all samples were observed by a field emission scanning electron microscopy (FESEM, ZEISS Sigma 300, Germany). Transmission electron microscopy (TEM), high-resolution lattices of the chosen materials, elected area electron diffraction (SAED), scanning TEM (STEM) images and element mappings were conducted by TEM (Talos F200x G2). X-ray photoelectron spectroscopy (XPS) was conducted upon the instrument of Thermo ESCALAB 250XI. Particle size of the samples was determined through a particle size analyzer (Malvern Mastersizer 2000, UK) and the true density of ball-milled samples was measured by a fully automatic density analyzer (AccuPyc II 1340, USA).

Cell preparation and testing

The electrochemical performance was evaluated with CR2025-type coin cells. The electrode slurries were prepared by mixing the active material, Super P and CMC-Na (sodium carboxymethyl cellulose, viscosity: 1000 – 1400 mPas, Aladdin)/PAA (polyacrylic acid, Mv ~ 3,000,000, Aladdin) in the mass ratio of 70:15:7.5:7.5 in deionized water. The working electrodes were fabricated by uniformly coating the slurries onto the Cu foil current collector with an active mass

loading of 0.7 – 1.4 mg·cm^{-2} corresponding to the area capacity of 2.1 – 2.6 mAh·cm^{-2}. The electrodes were then dried in vacuum at 80 °C for 12 h, followed by 150 °C for 1 h. the prepared electrode sheet was cut into small disk electrodes with a diameter of 12 mm. With the Li foil as a counter electrode, the coin cells were assembled in an argon-filled glovebox ($H_2O \leq 0.5$ ppm, $O_2 \leq 0.5$ ppm) (MBRAUN, Germany). The electrode separator was a Celgard 2400 membrane, and the electrolyte was a 1M $LiPF_6$ solution in a mixture of ethylene carbonate (EC) and dimethyl carbonate (DMC) at a volume ratio of 1:1 with 10% (volume) FEC (fluoroethylene carbonate) as the additive. The C-rate was determined by applying the current density of 100 mA·g^{-1} during the first cycle for all cells and the obtained lithiation capacity was adopted as 1C. Then, all cells were cycled under the current density of 0.2C in the voltage range of 0.01 – 1V versus Li/Li$^+$ since the second cycle.

Results and Discussion

1) Material Characterizations

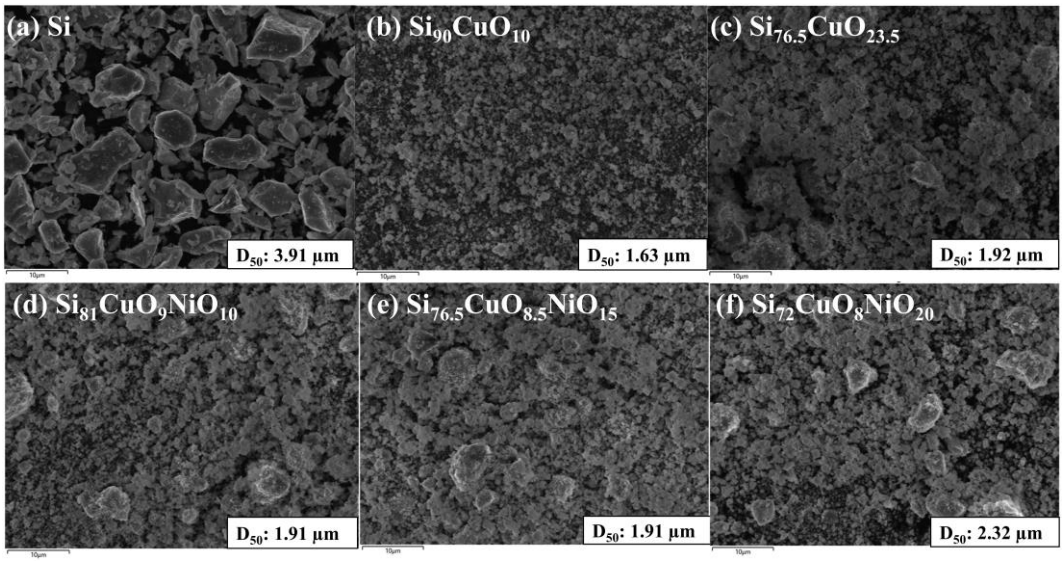

Figure 1. (a-h) SEM pictures of Si, Si-CuO and Si-CuO-NiO samples. The data of D_{50} for each sample were provided in the inserted white box on each picture.

The morphology of all the samples are shown in Figure 1 with the mean size (D_{50}) stated. The shape of the pristine Si particles is irregular under SEM with a relatively larger D_{50} of ~ 3.9 µm. As for all the other ball-milled samples, no obvious difference in morphology and particle size is observed under the chosen magnification with the D_{50} of 1.6 µm – 2.4 µm. The similar particle size here may help to ensure fair comparisons, i.e., the effect of particle sizes is minimized. Consequently, the influence of NiO additions on the electrochemical performances of the Si-based electrodes can be investigated and discussed in isolation.

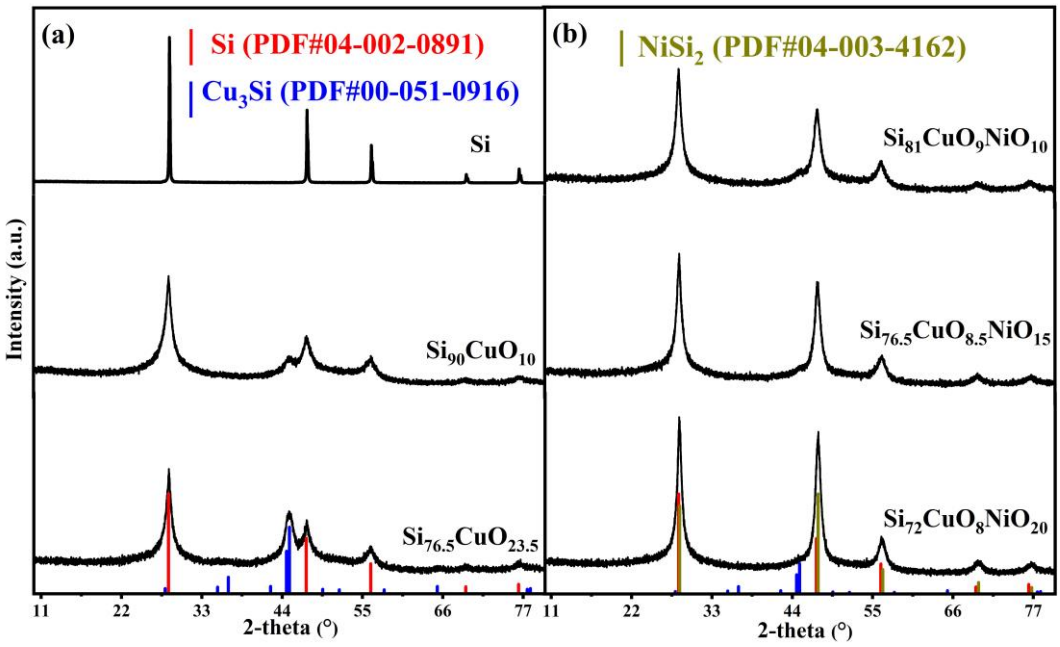

Figure 2. (a) XRD patterns of Si, Si-CuO samples and (b) XRD patterns Si-CuO-NiO samples

Figure 2 shows the diffraction patterns of pure Si and the ball-milled samples and the confirmation of phases is based on ICDD PDF-4+ released in 2009. There are no diffraction peaks related to CuO/NiO in Figure 2, indicating that both oxides have already reacted with Si and/or partly exist in the amorphous state. The diffractograms of pure Si and Si-CuO samples are shown in Figure 2(a). The former exhibits sharp peaks at 28.4°, 47.3°, 56.1°, 69.1° and 76.3 ° which are in line with crystalline Si

(PDF#04-002-0891). Differently, Si in the Si-CuO samples exhibits a significantly lower crystallinity, as supported by the peak broadening. Together with the Scherrer equation, the average grain size of Si in each sample can be estimated, such that an evident decrease in the grain size for pristine Si after the 4-hour milling, from ~80 nm in pure Si to ~ 8 nm in the Si-CuO samples. The two overlapped peaks at 44.5° and 44.9° in $Si_{90}CuO_{10}$ and $Si_{76.5}CuO_{23.5}$ indicate the formation of Cu_3Si (PDF#00-051-0916) with the grain size of ~ 7 nm and their relative intensities increases with the introduction of higher CuO contents.

The peaks related to Cu_3Si become inconspicuous in the diffractograms of the three Si-CuO-NiO samples in Figure 2(b), implying a higher amorphization degree of Cu_3Si [28, 29]. $NiSi_2$ is expected to be formed in this system with the diffraction peaks overlapping the ones of Si, and thus difficult to distinguish [32]. However, the relative peak intensities between these two phases are different, which can assist us to identify the existence of $NiSi_2$ [33]. Figure S1 shows the phase evolution of $Si_{72}CuO_8NiO_{20}$ during the milling process and with the extension of the milling time, the peaks related to NiO gradually become weaker, and eventually disappear after 4-hour milling. At the same time, the relative intensity of the peak at 47.3° is gradually increasing, which corresponds to the strongest peak of $NiSi_2$ (PDF#04-003-4126, referring to ICDD PDF-4+). Eventually, the ratio (100：91.7) of the peaks at 28.4° and 47.3° in $Si_{72}CuO_8NiO_{20}$ through 4-hour milling better consistent to the one (88.1：100) of $NiSi_2$ in the standard card, whereas this value in samples of pristine Si and Si-CuO are much closer to the theoretical value of Si (100：55.5). In addition, no peaks related to other Ni silicides are observed, further suggesting the most possibility of the crystalline $NiSi_2$ formation in the Si-CuO-NiO composites by the reaction of NiO and Si during the ball-milling process.

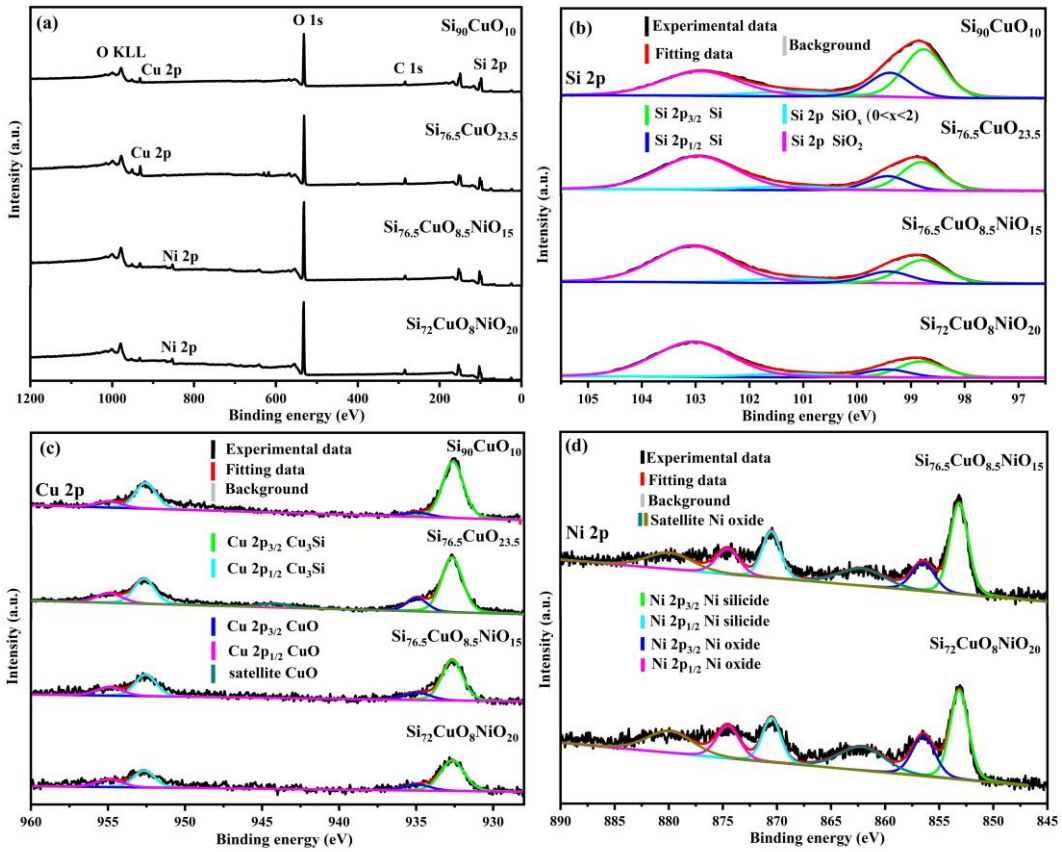

Figure 3. (a) XPS full spectra, (b) Si 2p spectra, (c) Cu 2p spectra of $Si_{90}CuO_{10}$, $Si_{76.5}CuO_{23.5}$, $Si_{76.5}CuO_{8.5}NiO_{15}$ and $Si_{72}CuO_8NiO_{20}$ samples. (d) Ni 2p spectra of $Si_{76.5}CuO_{8.5}NiO_{15}$ and $Si_{72}CuO_8NiO_{20}$ samples.

The XPS technique is employed to investigate the chemical state of different elements in the samples of $Si_{90}CuO_{10}$, $Si_{76.5}CuO_{23.5}$, $Si_{76.5}CuO_{8.5}NiO_{15}$ and $Si_{72}CuO_8NiO_{20}$. Figure 3(a) shows the full spectra of the samples and the peaks related to Si 2p, O 1s, Cu 2p and Ni 2p can be observed, confirming the existence of Si, O, Cu and Ni elements on the surface of the samples. Figure 3(b) presents the original XPS spectra as well as the results after fitting for Si 2p, revealing that the chemical state of Si element on the sample surfaces are similar. The peaks at around 98.8 eV and 99.4 eV are assigned to Si $2p_{3/2}$ and Si $2p_{1/2}$, most likely from elemental Si in pure Si and Cu_3Si [34, 35], respectively. Meanwhile, the peaks at around 103 eV and 101.2 eV are suggested to be contributed by SiO_2 and SiO_x ($0<x<2$) [30, 34], respectively. Obviously, SiO_2, as the major form among all kinds of Si oxides, is detected on the surface of the samples. It is supported by the XPS fitting data that the

SiO_2 content follows a monotonical increase with the amount of the metal oxides. This correlation implies that a part of the SiO_2 formation on the particle surface may partly be contributed by the reactions between Si and CuO/NiO, especially since the Ar condition is maintained during the milling process

Figure 3(c) presents the Cu 2p spectra of the samples. The peaks at around 932.6 eV and 952.6 eV shows that the chemical state of Cu element on the surface is mainly in its zero valence instead of +2 valence, further proving the reduction reaction between CuO and Si during the ball-milling process. Due to the identical XPS binding energy of Cu $2p_{3/2}$ in Cu_3Si and pure Cu [35], in conjunction with the XRD results, it is suggested that the two peaks most likely originate from the elemental Cu of produced Cu_3Si. The Ni 2p spectra of $Si_{76.5}CuO_{8.5}NiO_{15}$ and $Si_{72}CuO_8NiO_{20}$ can be seen in Figure 3(d). The peaks at around 853.1 eV and 870.5 eV are assigned to Ni $2p_{3/2}$ and Ni $2p_{1/2}$ of Ni silicide [36, 37], respectively. We find the XPS binding energies of these two peaks are closer to the ones of $Ni_{31}Si_{12}$ or Ni_2Si instead of $NiSi_2$, in which the peaks of Ni $2p_{3/2}$ and Ni $2p_{1/2}$ are around 854.6 eV and 871.8 eV [36, 37], indicating that NiO has probably been reduced by Si. Whereas the mechanism of how Ni-rich silicides form on the surface has not been fully understood at this moment , thereby warrants further investigations. In addition, the peaks assigned to CuO [30] and NiO [38] in the Cu 2p and Ni 2p spectra can be also found in Figures 3(c-d) indicating that there might be the minor amorphous metal oxides remaining in the Si-CuO and the Si-CuO-NiO samples, which are not completely consumed after our milling process. To sum up, the XPS results demonstrate the existence of Si oxides, elemental Si and Cu on the surface of the chosen samples with minor residual metal oxides, whereas the peaks related to $NiSi_2$ are not detected in this study.

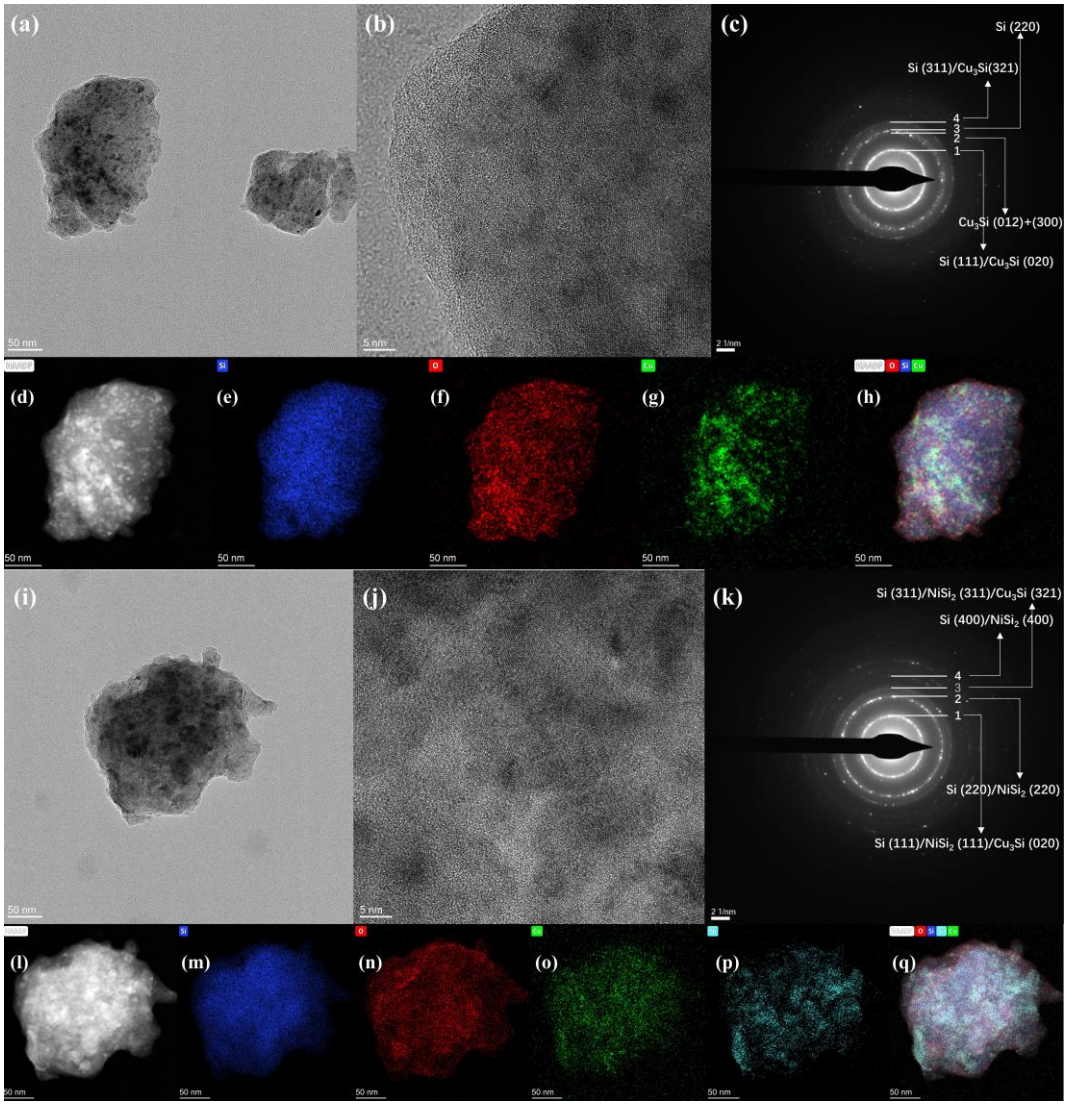

Figure 4. TEM images of $Si_{76.5}CuO_{23.5}$ and $Si_{76.5}CuO_{8.5}NiO_{15}$ samples: (a) and (i) BF images, (b) and (j) HREM images, and (c) and (k) SAED patterns; STEM images of $Si_{76.5}CuO_{23.5}$ and $Si_{76.5}CuO_{8.5}NiO_{15}$ samples: (d) and (l) STEM images, (e) and (m) Si maps (dark blue color), (f) and (n) O maps (red color), (g) and (o) Cu maps (green color), (p) Ni maps (only for $Si_{76.5}CuO_{8.5}NiO_{15}$, light blue color), (h) Si, O and Cu substitution overlaps for $Si_{76.5}CuO_{23.5}$ and (q) Si, O, Cu and Ni substitution overlaps for $Si_{76.5}CuO_{8.5}NiO_{15}$.

In order to confirm the microstructure and the element distribution, the typical samples of $Si_{76.5}CuO_{23.5}$ and $Si_{76.5}CuO_{8.5}NiO_{15}$ are chosen to undergo TEM and STEM tests as well as considering their same metal oxides proportion. According to the bright field (BF) images shown in Figures 4(a, i) and HRTEM images of Figures 4(b, j), the ball-milled Si-based particles are composed of many dispersed nano-crystallites and some amorphous regions (among the crystallites or on the edge of the particles). These amorphous regions in the two samples are possibly amorphous Si

oxides or residual metal oxides based on the XRD and XPS results. By analyzing the SAED pattern in Figures 4(c, k), we could get to know the nano-crystallites derive from Si, Cu_3Si and $NiSi_2$, respectively. As mentioned before, Si and $NiSi_2$ have similar crystalline structures with the almost identical lattice parameter [32]. Thus, they are considered to be represented by the same diffraction rings. No other Ni silicides are observed from the diffraction rings in Figure 4(k). Combing with the XRD results, it is suggested that $NiSi_2$ exists as the only crystalline Ni silicide in $Si_{76.5}CuO_{8.5}NiO_{15}$ among various Si-Ni compounds after our ball-milling process. Besides, the element distribution in ball-milled Si-based alloys is the other key factor since a better cycling performance is expected from a sample with a better homogeneity [6, 38]. The bright regions in STEM images (Figure 4(d) and 4(l)) denotes the doped metal elements. The element mapping and the related substitution overlaps (Figures 3(d-h, l-q)) further confirm the existence of Si, O, Cu and Ni elements, consistent to the XPS results. Clearly, all the elements in the $Si_{76.5}CuO_{8.5}NiO_{15}$ sample are homogenously distributed. However, the Cu element in $Si_{76.5}CuO_{23.5}$ seems to exhibit agglomerations to some extent within the scanned region.

Herein, combing the results of XRD, XPS, TEM and STEM, we draw the conclusion that after the 4-hour ball-milling process for the Si-CuO and Si-CuO-NiO composites, the obtained samples mainly consist of nanocrystalline Si, doped metal silicide, and amorphous Si oxides while a uniform element distribution is observed for the $Si_{76.5}CuO_{8.5}NiO_{15}$ sample.

2) Electrochemical characterizations

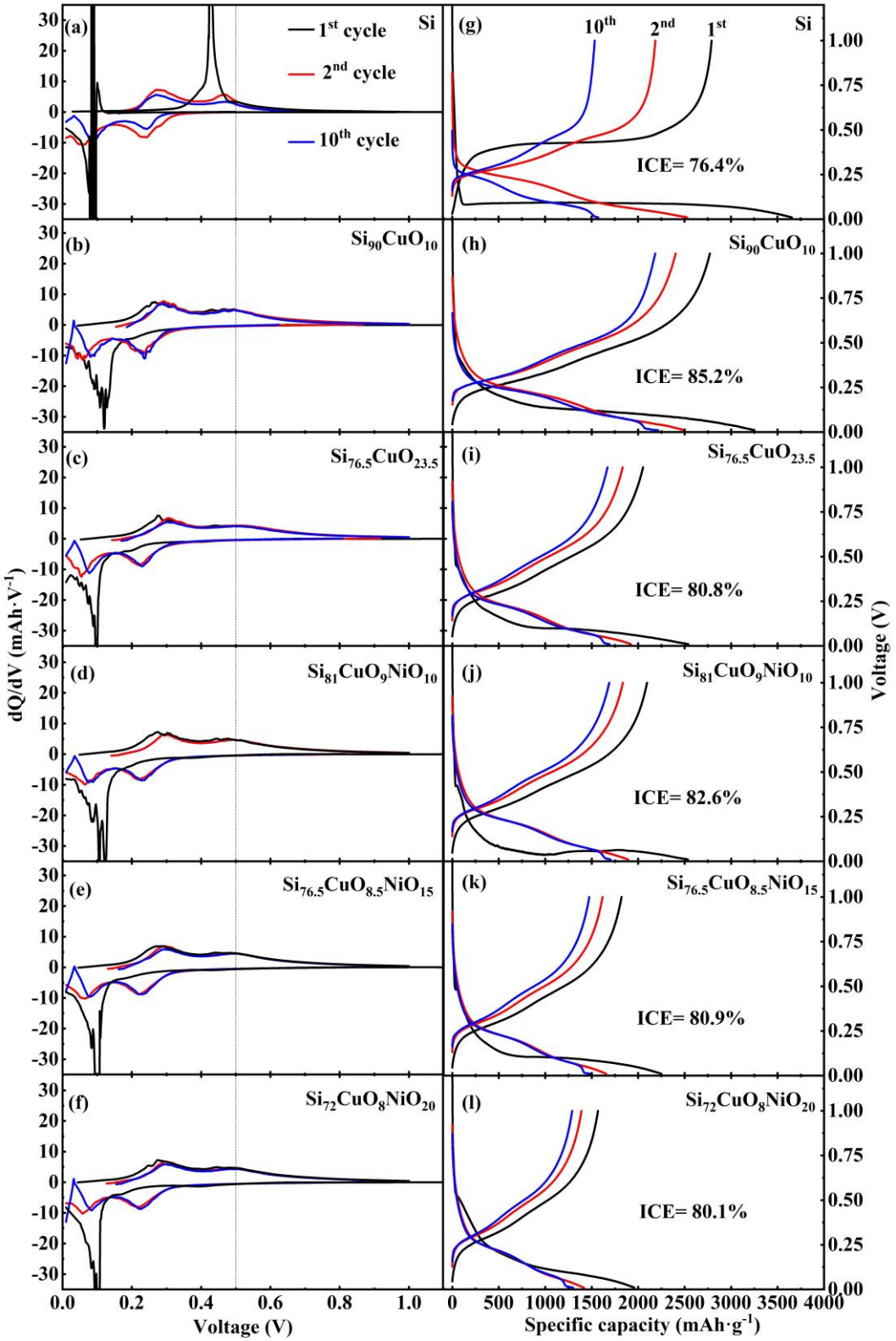

Figure 5. (a-f) dQ/dV-voltage curves of the 1st, 2nd and 10th cycle of Si, Si-CuO and Si-CuO-NiO samples, and (g-l) their corresponding voltage-capacity curves.

The electrochemical behaviors of Si, Si-CuO and Si-CuO-NiO samples are investigated by presenting their differential capacity-voltage (dQ/dV) curves in Figures 5(a-f) and corresponding voltage-capacity curves in Figures 5(g-l). Evidently, the 1st lithiation for all samples show distinctive features from the subsequent cycles, giving a pronounced lithiation peak at around 0.1 V versus Li/Li^+ in the dQ/dV curves corresponding to a lithiation plateau at the same potential in the voltage-capacity curves. This lithiation peak is indicative of a two-phase co-existence region of cr-Si and amorphous Li_xSi ($0<x\leq3.5$) [39, 40]. Compared with pure Si, this peak becomes broader for the Si-CuO and Si-CuO-NiO samples, which may be due to the microstructure change of the ball-milled Si particles with lower crystallinity [19, 20].

For the 1st delithaition, only one noticeable peak at ~ 0.43 V in the dQ/dV curve of pristine Si can be seen (Figure 5a), whereas two pronounced peaks at around 0.3 V and 0.5 V vs. Li/Li^+ exist in the dQ/dV curves of the Si-CuO and Si-CuO-NiO samples, representing the transformation from a-$Li_{3.5}Si$ to a-Li_2Si and from a-Li_2Si to a-Si, respectively [39, 40]. The appearance of 0.43 V delithiation peak is a sign of cr-$Li_{3.75}Si$ generated in the Si bulk, which is considered detrimental to the electrochemical performance as a result from the mismatched volume change in the phase boundary between cr-$Li_{3.75}Si$ and amorphous Li_xSi alloy [41]. Correspondingly, pristine Si has a lowest initial coulombic efficiency (ICE) of 76.4 % (Figure 5(g)) in this study suggested to be partly caused by the generation of cr-$Li_{3.75}Si$ leading to bigger fracture of the electrode with more Li^+ trapped in the Si bulk during the first delithiation [41]. On the other hand, this peak becomes obscure in the dQ/dV curves of the Si-CuO and Si-CuO-NiO samples mainly ascribed to stress-voltage coupling induced by formed Cu_3Si and $NiSi_2$ [8, 42, 43]. These inactive phases can impose a compressive stress on the expanded Si bulk during the lithiation, for example, a

higher compressive stress of 1.5 GPa will negatively shift the lithiation potential as much as 200 mV to completely avoid the formation of cr-$Li_{3.75}Si$ [2, 8, 42, 43]. For the ball-milled samples, a negative correlation is observed between the ICEs and the metal oxides content. The up to 28% addition of metal oxides leads to an ICE variation from 85.2 % to 80.1% (Figures 5(h-l)). This correlation could partly be caused by the introduction of more oxides, such as the irreversible lithiation of the formed Si oxides [22] and/or native metal oxides of the as prepared samples [44, 45]. The drop of ICE can be made up by the prelithiation technology [46].

Since the second cycle, two broad lithiation peaks at around 0.06 V and 0.23 V vs. Li/Li^+ appear in the dQ/dV curves for all the samples, corresponding to a pair of sloping plateaus in the voltage-capacity curves. These two peaks are believed to be indicative of the formation of amorphous Li_2Si and $Li_{3.5}Si$ [47], while the delithiation peak for cr-$Li_{3.75}Si$ is always absent among the ball-milled samples in the later cycles similar with the 1^{st} delithiation. In brief, the ball-milled Si-CuO and Si-CuO-NiO samples still show the lithiation feature of cr-Si during the first cycle but the generation of cr-$Li_{3.75}Si$ is effectively hindered, and thereby positively affecting the electrochemical performance [41]. The introduction of NiO does not seem to vary the underlying reaction mechanisms for the ball-milled Si-CuO and Si-CuO-NiO samples during the first 10 cycles.

Table 1. Reversible capacity of 1st and 100th cycles, 100th-cycle capacity retention and ACE of Si, Si-CuO and Si-CuO-NiO samples.

Sample	1st reversible capacity (mAh·g^{-1})	100th reversible capacity (mAh·g^{-1})	Capacity retention of 100th-cycle (%, based on 2nd cycle)	ACE (%, based on 2nd-cycle)
Si	2792	453	20.7	98.47
$Si_{90}CuO_{10}$	2771	1781	74.1	98.89
$Si_{76.5}CuO_{23.5}$	2052	1092	59.6	98.94
$Si_{81}CuO_9NiO_{10}$	2095	1471	80.1	99.06
$Si_{76.5}CuO_{8.5}NiO_{15}$	1821	1366	84.5	99.23
$Si_{72}CuO_8NiO_{20}$	1568	1208	86.9	99.40

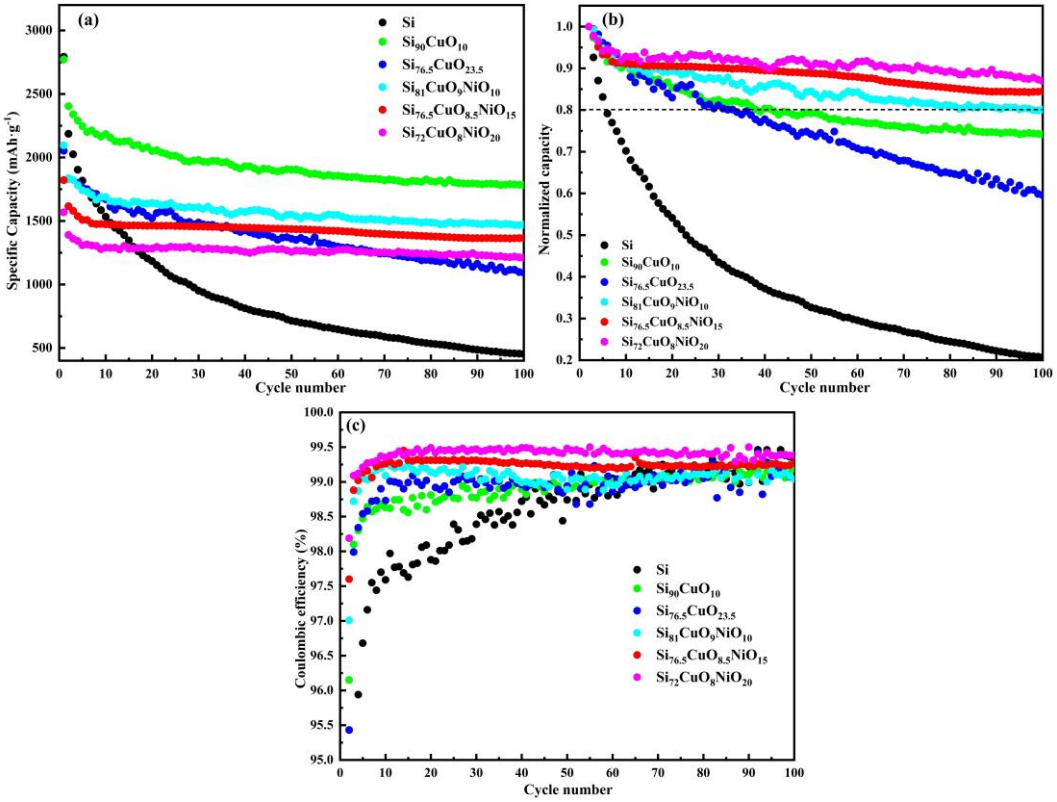

Figure 6. (a) Specific delithiation capacity vs. cycle number, (b) normalized delithiation capacity (with respect to the second cycle) vs. cycle number and (c) the coulombic efficiency of of Si, Si-CuO and Si-CuO-NiO samples.

Next, the cycle stabilities of the Si, Si-CuO and Si-CuO-NiO samples are evaluated by presenting the 100-cycle data in Figures 6(a-c), with the quantitative data listing in Table 1. To start with, the highest initial delithiation capacity is observed for the pristine Si and the capacity decreases by introducing more metal oxides, following a monotonical trend. The formation of the metal silicides and Si

oxides with limited reversible capacity (e.g., $Cu_3Si/NiSi_2$ or SiO_x [10, 24, 42]), is suggested to be responsible for the capacity decrease. However, the cycling stability of pristine Si is the poorest with a capacity retention of only 20.7% after 100 cycles (Figure 6(b)). When a 10% addition of CuO via ball-milling into Si bulk, it is found to significantly improve the cycling performance, giving 74.1% capacity retention after 100 cycles, consistent to the previous reports [28, 29]. As the CuO content further rises to 23.5%, the cycle performance of $Si_{76.5}CuO_{23.5}$ unexpectedly becomes worse showing a 100^{th}-cycle capacity retention of 59.6 %. This result implies solely adding an excessive amount of CuO (23.5%) element could somehow deteriorate the cycle performance of the electrode, ultimately limiting the further improvement of capacity retention [38]. On the other hand, the poorer cycle stability of $Si_{76.5}CuO_{23.5}$ suggests that the Cu/CuO content should be carefully adopted, especially since the Cu/CuO addition is considered a common approach for improvement of the Si-based anodes [28, 30, 38, 48]. Thus, the core strategy of this study is to replace a part of CuO with NiO in order to avoid this issue in the single Si-CuO system. In sharp contrast, the addition of NiO takes significant positive effect to the electrochemical performance. The capacity retention after 100 cycles of Si-CuO-NiO samples continuously increase with more introduction of NiO, from 80.1% in $Si_{81}CuO_9NiO_{10}$ to 86.9% in $Si_{72}CuO_8NiO_{20}$. Moreover, the average coulombic efficiencies (ACE) in Si-CuO-NiO samples are also noticeably enhanced (Figure 6(c)), with the highest one observed in the $Si_{72}CuO_8NiO_{20}$, giving an ACE of ~ 99.4% (Table 1). It highlights the importance of the role of NiO addition and confirms introducing a proper amount of NiO into the Si-CuO system could indeed be an effective method to improve the electrochemical performance of Si-based alloy anodes.

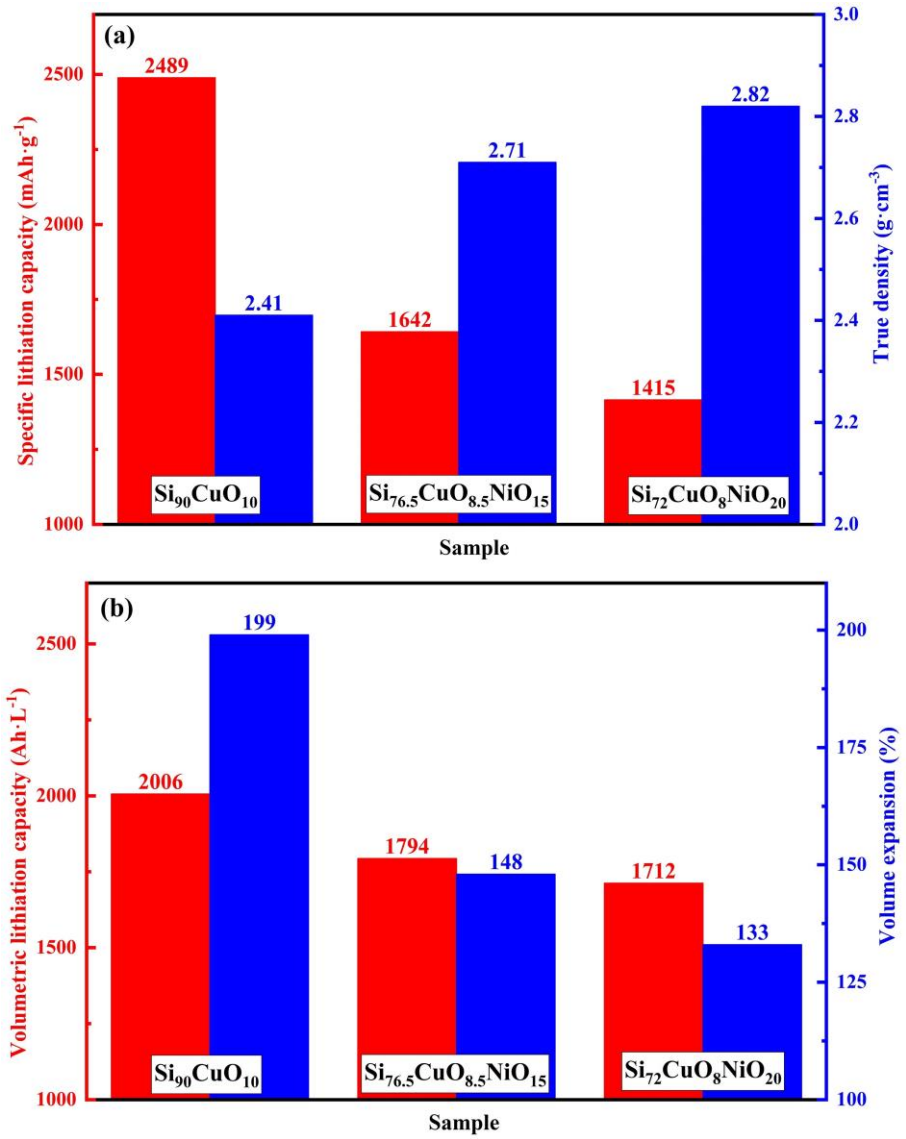

Figure 7. (a) 2nd specific lithiation capacity and true density, and (b) corresponding volumetric lithiation capacity and volume expansion percentage of $Si_{90}CuO_{10}$, $Si_{76.5}CuO_{8.5}NiO_{15}$ and $Si_{72}CuO_8NiO_{20}$.

We assume the improved capacity retention and ACE are mainly the role played by reduced the structural change in Si-CuO-NiO samples due to the formation of $NiSi_2$ consuming more active Si than Cu_3Si. In order to estimate, to what extent, the addition of metal oxides could suppress the volume expansion of Si in the samples of $Si_{90}CuO_{10}$, $Si_{76.5}CuO_{8.5}NiO_{15}$ and $Si_{72}CuO_8NiO_{20}$, the following equation presented elsewhere is employed [12]:

$$§ = (k * \rho_{alloy} * c_{alloy}) / F * 100\%$$

where § is the volume expansion of the Si-based composite anodes in percentage, k is

the molar volume of lithium in active materials (here is 8.9 mL/mol [12]), ρ_{alloy} is the true density of the unlithiated Si-based composites in g/mL, c_{alloy} is the lithiation specific capacity the Si-based alloy anodes in Ah/g (considering the contribution of SEI and lithium silicates formation to the 1st lithiation capacity, here we used the second lithiation capacity) and F is Faraday's number ($\approx$ 26.802 Ah/mol). Considering the obvious negative influence of excessive CuO on the cycle performance, $Si_{76.5}CuO_{23.5}$ is excluded from the calculation. The true densities and 2nd lithiation capacities for the chosen samples are measured and shown in Figure 7(a). According to the aforementioned equation, Figure 7(b) presents the calculated volume expansions (in blue columns) of three different samples. Generally, the samples with NiO addition exhibit less volume expansions (148% for 15% NiO and 133% for 20% NiO), as compared to $Si_{90}CuO_{10}$ with 199%. The alleviated volume changes of $Si_{76.5}CuO_{8.5}NiO_{15}$ and $Si_{72}CuO_8NiO_{20}$ are beneficial to lessen crack formation and exposure of fresh Si surface, thus inhibiting secondary SEI and/or continues breakdown of electrolyte [4-6]. At the same time, relatively mild volume change is also helpful to keep the good electrical contact between the active material and conductive matrix (the current collector and/or conductive carbon) for long-term cycling [2]. Morever, the volumetric capacity of three samples were also calculated using the obtained data of c_{alloy}, ρ_{alloy} and § [49] summarized in Figure 7(b) with red columns. It can be found that different from the gravimetric specific capacity, there is a much smaller reduction on the volumetric specific capacity for $Si_{76.5}CuO_{8.5}NiO_{15}$ and $Si_{72}CuO_8NiO_{20}$. In a real application, the improved energy density for a full cell with limited space accommodating electrode materials is easier to be achieved via using high volumetric capacity Si-based alloy as anodes [12]. At the same time, over 1700 $Ah \cdot L^{-1}$ of the volumetric lithiation capacity for $Si_{76.5}CuO_{8.5}NiO_{15}$ and

$Si_{72}CuO_8NiO_{20}$ is considerably attractive compared with graphite of only 719 $Ah{\cdot}L^{-1}$ [2]. Considering the cost, we did not continue to increase the mass of NiO and the ratio of CuO to NiO in the composites is expected to be optimized in the further work.

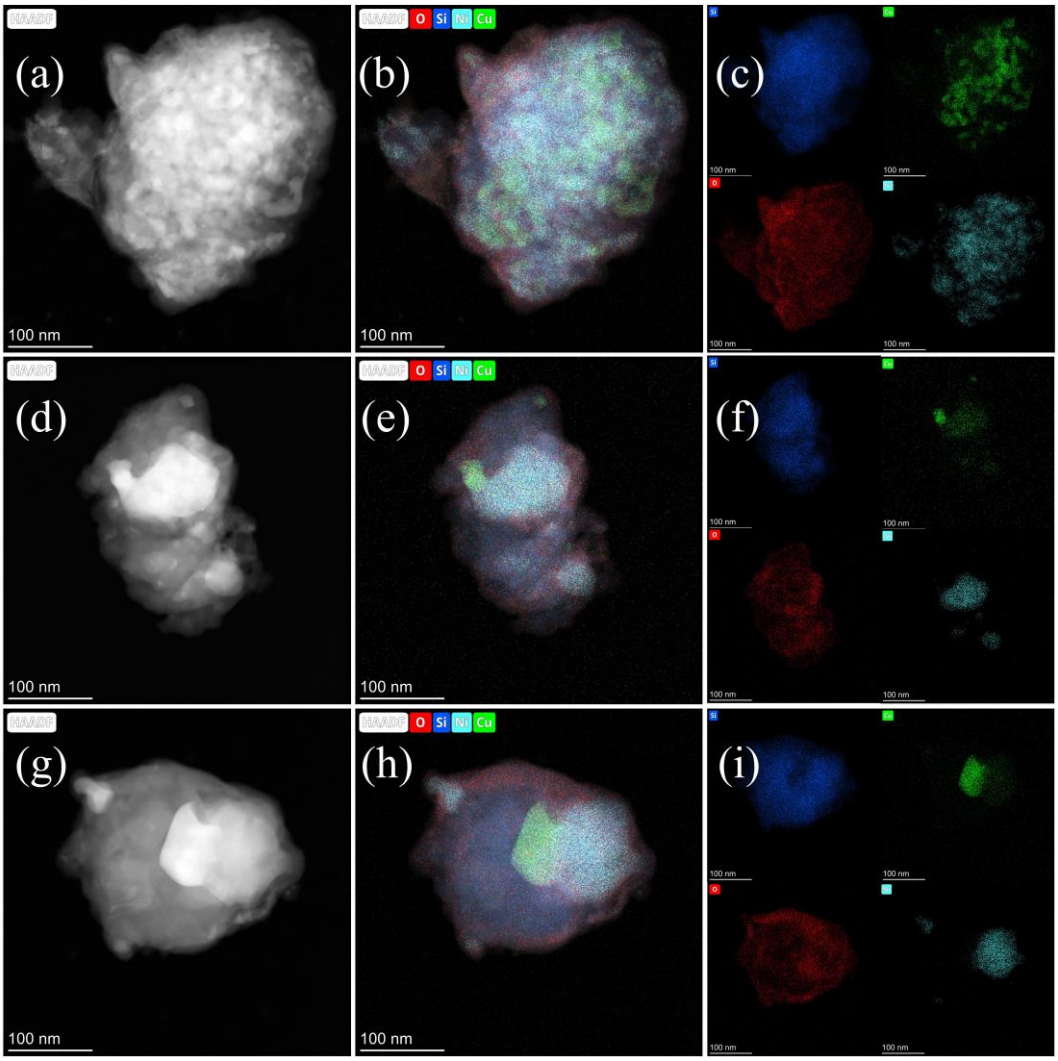

Figure 8. BF images ((a), (e) and (i)), STEM images ((b), (f) and (j)), element substitution overlaps ((c), (g) and (k)) and element maps ((d), (h) and (l)) of $Si_{72}CuO_8NiO_{20}$-600, $Si_{72}CuO_8NiO_{20}$-800 and $Si_{72}CuO_8NiO_{20}$-900. Si map (dark blue color), O map (red color), Cu map (green color) and Ni map (light blue color).

Lastly, we chose $Si_{72}CuO_8NiO_{20}$ to test the thermal stability due to the best comprehensive performance in this study. Generally, the annealing temperature of coating a carbon layer depends on the types of carbon sources and coating methods with a wide temperature range, for example, changing from 400 °C to 900 °C [9, 47, 48, 50-53]. Because there will be an obvious grain growth for Si-based anodes since

600 °C [54], it is chosen as an initial sintering temperature followed by 800 °C and 900 °C with 3 hours. The XRD patterns of sintered samples are shown in Figure S2(a). It can be seen that all diffraction peaks of sintered samples become sharper indicating the improvement of the crystallinity and the grain size. The peaks at 44.5° and 44.9° related to Cu_3Si become more recognizable and separated distinctively. We calculated the grain size of Cu_3Si using the Scherrer equation for the three sintered samples with an increase from ~ 37 nm to ~ 45 nm (seen in Figure S2 (b)). Besides, the peaks assigned to Si oxides still cannot be found in the Figure S2 (a) implying the stable amorphous structure for Si oxides even going through the high-temperature annealing process (no more than 900 °C). This property of amorphous Si oxides is thought to be helpful to maintain the cycle stability [22]. TEM and STEM were conducted to characterize the change of microstructure and element distribution in the sintered $Si_{72}CuO_8NiO_{20}$. Figure S3 shows the BF images and the HRTEM images of the chosen regions. The microstructure of $Si_{72}CuO_8NiO_{20}$-600 is very similar with the one of $Si_{76.5}CuO_{8.5}NiO_{15}$ consisting of uniformly distributed nano-crystallites and amorphous regions. However, it has a noticeable transformation of the microstructure for $Si_{72}CuO_8NiO_{20}$-800 and $Si_{72}CuO_8NiO_{20}$-900, where the distribution of metal silicides starts to agglomerate and the rich-Cu_3Si or rich-$NiSi_2$ regions appear. This phenomenon is further confirmed by STEM results (seen in Figure 8). Overall, the state of element distribution in $Si_{72}CuO_8NiO_{20}$-600 still maintains good dispersion without apparent agglomeration. When the annealing temperature is up to 800 °C and 900 °C, the distribution of Cu and Ni elements become more centralized corresponding to the rich-Cu_3Si or rich-$NiSi_2$ regions in Figure S3. Such evolution of element distribution in Si bulk is not what we expected, which is predicted to influence the electrochemical behaviors and performance.

The dQ/dV curves of the sintered samples and corresponding voltage-capacity curves are shown in Figure S4. There is no obvious difference in dQ/dV curves and voltage-capacity curves between $Si_{72}CuO_8NiO_{20}$ and $Si_{72}CuO_8NiO_{20}$-600. However, the shape of these curves for $Si_{72}CuO_8NiO_{20}$-800 and $Si_{72}CuO_8NiO_{20}$-900 become closer to the ones of pristine Si due to the higher crystallinity. The peak at ~ 0.43 V representing cr-$Li_{3.75}Si$ delithiation appears in the first dQ/dV curves of $Si_{72}CuO_8NiO_{20}$-800 and $Si_{72}CuO_8NiO_{20}$-900 but with the exception of $Si_{72}CuO_8NiO_{20}$-600. It may be because the formation of rich-Cu_3Si or rich-$NiSi_2$ regions decreases the contact areas between Si grains and metal silicides causing inadequate compressive stress to suppress cr-$Li_{3.75}Si$ generation during the lithiation. Then, we calculated the capacity percentage derived from cr-$Li_{3.75}Si$ delithiation during the first cycle for Si, $Si_{72}CuO_8NiO_{20}$, $Si_{72}CuO_8NiO_{20}$-600, $Si_{72}CuO_8NiO_{20}$-800 and $Si_{72}CuO_8NiO_{20}$-900 via the method provided by the literature [43] (the result and detailed description about the calculation are shown in Figure S5). Obviously, such percentage for $Si_{72}CuO_8NiO_{20}$ and $Si_{72}CuO_8NiO_{20}$-600 is in a close level with ~ 3 %, whereas it has a significant increase for $Si_{72}CuO_8NiO_{20}$-800 and $Si_{72}CuO_8NiO_{20}$-900 with ~ 35% but still less than pristine Si with the percentage over 60 %. This confirms again that the introduction of CuO and NiO can effectively suppress the formation of cr-$Li_{3.75}Si$ but the effect can be influenced by the distribution state of the metal elements or silicides in the Si bulk. The 100-cycle performance of sintered samples are provided by Figure 9 and $Si_{72}CuO_8NiO_{20}$-600 performs the highest capacity retention with ~ 91.2 % even more than the one (~ 86.9 %) in $Si_{72}CuO_8NiO_{20}$. It is speculated by the improved crystallinity of metal silicides in $Si_{72}CuO_8NiO_{20}$-600 providing better electrical conductivity during the cycling [38] or the more sufficient reaction between Si and metal oxides via the sintering treatment. The value for

$Si_{72}CuO_8NiO_{20}$-800 and $Si_{72}CuO_8NiO_{20}$-900 have a different degree of decline. Especially, the cycle performance for $Si_{72}CuO_8NiO_{20}$-900 become very worse with the capacity retention of only ~ 67.2 %. We ascribe the results to the following reasons: 1) The generation of more cr-$Li_{3.75}Si$ in the initial stage may accelerate the fragmentation of the Si bulk and the crack formation on the surface of the electrode leading to the capacity loss [41]; The ball-milled precursors cannot withstand the high-temperature annealing treatment of 900 °C, where the formed metal silicide clusters reduce the limitation to the growth of the Si grains. The larger grain size of Si is usually considered not conducive to maintain a good cycle stability [14, 15]; 3) Such clusters may impose uneven compressive or tensile stress to Si bulk during the lithiation (expanded) or delithiation (contracted) process. Accordingly, it is more likely to cause the structural break to the Si bulk with the mechanical failure, poor electrical contact, unstable SEI and increased impedance resistance [5, 6]. Therefore, we expect a post carbon coating treatment with the annealing temperature no more than 800 °C may obtain an improved cycle performance for the ball-milled $Si_{72}CuO_8NiO_{20}$ precursor.

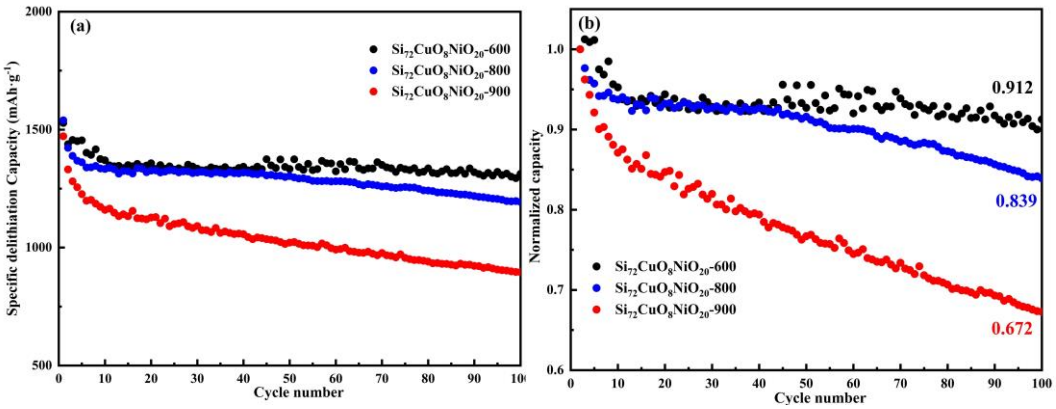

Figure 9. (a) Specific delithiation capacity vs. cycle number and normalized delithiation capacity (with respect to the second cycle) vs. cycle number of $Si_{72}CuO_8NiO_{28}$-600, $Si_{72}CuO_8NiO_{28}$-800 and $Si_{72}CuO_8NiO_{28}$-900.

Conclusions

In this study, NiO is adopted to modify the Si-CuO alloy anodes in LIBs via a HEBM method. The XRD, XPS and TEM results reveal the obtained Si-CuO-NiO samples mainly consists of nanocrystalline Si, doped metal silicides and amorphous Si oxides and there is a uniform distribution of each element in $Si_{76.5}CuO_{8.5}NiO_{15}$. The electrochemical analysis indicate Si-CuO-NiO samples do not show remarkable differences in the reaction mechanisms, as compared to the Si-CuO samples. The formation of cr-$Li_{3.75}Si$ in the lithiation process is effectively suppressed in both systems. However, a higher CuO addition (23.5%) is observed to severely deteriorate the cycle performance of the Si-based anode limiting the improvement of the cycle stability. Using NiO to replace a part of CuO is suggested to be effective in mitigating this issue, giving an enhanced cycle performance with less volume change and higher coulombic efficiency. In addition, the testing results of the thermal stability manifests the ball-milled Si-CuO-NiO precursors are more suitable to be coated a carbon layer under the annealing temperature no more than 800 °C.

Conflicts of interest

There are no conflicts to declare.

Acknowledgments

Thanks to Dr. Zhou Ruitao for the helpful discussion and supports from Shiyanjia Lab (www. Shiyanjia.com) for the testing of TEM/HRTEM.

References

[1] P. Li, H. Kim, S.-T. Myung, Y.-K. Sun, Diverting Exploration of Silicon Anode into Practical Way: A Review Focused on Silicon-Graphite Composite for Lithium Ion Batteries, Energy Storage Materials, 35 (2021) 550-576.
[2] M.N. Obrovac, Si-alloy negative electrodes for Li-ion batteries, Current Opinion in Electrochemistry, 9 (2018) 8-17.
[3] L.J.K. M. N. Obrovac, Reversible Cycling of Crystalline Silicon Powder, J. Electrochem. Soc., 154 (2007) 6.
[4] Z.J. Du, R.A. Dunlap, M.N. Obrovac, High Energy Density Calendered Si Alloy/Graphite Anodes, J. Electrochem. Soc., 161 (2014) A1698-A1705.
[5] S.M. Cao, M.H. Tahmasebi, J.C. Bennett, M.N. Obrovac, Si-TiN alloy anode materials prepared by reactive N-2 gas milling: thermal stability and electrochemistry in Li-cells, Electrochim. Acta, 396 (2021) 10.
[6] S.M. Cao, J.C. Bennett, Y.K. Wang, S. Gracious, M. Zhu, M.N. Obrovac, Si-TiN alloy Li-ion battery anode materials prepared by reactive N-2 gas milling, J. Power Sources, 438 (2019) 8.
[7] M. Kim, Z. Yang, I. Bloom, Review—The Lithiation/Delithiation Behavior of Si-Based Electrodes: A Connection between Electrochemistry and Mechanics, J. Electrochem. Soc., 168 (2021).
[8] M. Ruttert, V. Siozios, M. Winter, T. Placke, Mechanochemical Synthesis of Fe–Si-Based Anode Materials for High-Energy Lithium Ion Full-Cells, ACS Applied Energy Materials, 3 (2019) 743-758.
[9] S.-S. Lee, K.-H. Nam, H. Jung, C.-M. Park, Si-based composite interconnected by multiple matrices for high-performance Li-ion battery anodes, Chemical Engineering Journal, 381 (2020).
[10] Z.J. Du, T.D. Hatchard, P. Bissonnette, R.A. Dunlap, M.N. Obrovac, Electrochemical Activity of Nano-NiSi2 in Li Cells, J. Electrochem. Soc., 163 (2016) A2456-A2460.
[11] Z.J. Du, T.D. Hatchard, R.A. Dunlap, M.N. Obrovac, Combinatorial Investigations of Ni-Si Negative Electrode Materials for Li-Ion Batteries, J. Electrochem. Soc., 162 (2015) A1858-A1863.
[12] M.N. Obrovac, L. Christensen, D.B. Le, J.R. Dahnb, Alloy design for lithium-ion battery anodes, J. Electrochem. Soc., 154 (2007) A849-A855.
[13] M.N. Obrovac, L. Christensen, D.B. Le, J.R. Dahn, Alloy Design for Lithium-Ion Battery Anodes, J. Electrochem. Soc., 154 (2007).
[14] M.T. McDowell, S.W. Lee, J.T. Harris, B.A. Korgel, C. Wang, W.D. Nix, Y. Cui, In situ TEM of two-phase lithiation of amorphous silicon nanospheres, Nano Lett, 13 (2013) 758-764.
[15] X.H. Liu, L. Zhong, S. Huang, S.X. Mao, T. Zhu, J.Y. Huang, Size-Dependent Fracture of Silicon Nanoparticles During Lithiation, Acs Nano, 6 (2012) 1522-1531.
[16] S.M. Cao, S. Gracious, J.C. Bennett, M.N. Obrovac, Synthesis, Lithium Insertion and Thermal Stability of Si-Mo Alloys, J. Electrochem. Soc., 167 (2020).
[17] Y.J. Liu, C. Bennett, M.N. Obrovac, Ball Milled Si-W Alloys: Part II. Thermal Behavior and Performance in Li Cells, J. Electrochem. Soc., 166 (2019) A2791-A2796.
[18] Y.D. Cao, J.C. Bennett, R.A. Dunlap, M.N. Obrovac, Li Insertion in Ball Milled Si-Mn Alloys, J. Electrochem. Soc., 165 (2018) A1734-A1740.

[19] Y.K. Wang, S.M. Cao, M. Kalinina, L.T. Zheng, L.J. Li, M. Zhu, M.N. Obrovac, Lithium Insertion in Nanostructured Si1-xTix Alloys, J. Electrochem. Soc., 164 (2017) A3006-A3010.
[20] Z.J. Du, S.N. Ellis, R.A. Dunlap, M.N. Obrovac, NixSi1-x Alloys Prepared by Mechanical Milling as Negative Electrode Materials for Lithium Ion Batteries, J. Electrochem. Soc., 163 (2016) A13-A18.
[21] Y. Zhang, C. Zhu, Z. Ma, Si@Cu3Si nano-composite prepared by facile method as high-performance anode for lithium-ion batteries, Journal of Alloys and Compounds, 851 (2021).
[22] Y.J. Liu, M. Charlton, J. Wang, J.C. Bennett, M.N. Obrovac, Si85Fe15Ox Alloy Anode Materials with High Thermal Stability for Lithium Ion Batteries, J. Electrochem. Soc., 168 (2021) 9.
[23] X.Y. Zhao, R.J. Sanderson, M.A. Al-Maghrabi, R.A. Dunlap, M.N. Obrovac, Electrochemistry of Sputtered and Ball Milled Si-Fe-O Alloys in Li Cells, J. Electrochem. Soc., 164 (2017) A1165-A1172.
[24] Z. Liu, Q. Yu, Y. Zhao, R. He, M. Xu, S. Feng, S. Li, L. Zhou, L. Mai, Silicon oxides: a promising family of anode materials for lithium-ion batteries, Chem Soc Rev, 48 (2019) 285-309.
[25] Y.D. Cao, J.C. Bennett, R.A. Dunlap, M.N. Obrovac, A Simple Synthesis Route for High-Capacity SiOx Anode Materials with Tunable Oxygen Content for Lithium-Ion Batteries, Chemistry of Materials, 30 (2018) 7418-7422.
[26] A. Hohl, T. Wieder, P.A. van Aken, T.E. Weirich, G. Denninger, M. Vidal, S. Oswald, C. Deneke, J. Mayer, H. Fuess, An interface clusters mixture model for the structure of amorphous silicon monoxide (SiO), J Non-Cryst Solids, 320 (2003) 255-280.
[27] L. Shi, Y. Li, Y. Xing, R. Lin, G. Cheng, J. Ding, K.H. Lam, SiOx microparticles embedded into 3D wrinkled N, S co-doped multilayer graphene sheets as a high-performance anode for long-life full lithium-ion batteries, Electrochim. Acta, 390 (2021).
[28] S.C. Hou, T.Y. Chen, Y.H. Wu, H.Y. Chen, X.D. Lin, Y.Q. Chen, J.L. Huang, C.C. Chang, Mechanochemical synthesis of Si/Cu3Si-based composite as negative electrode materials for lithium ion battery, Sci Rep, 8 (2018) 12695.
[29] Y.-H. Wu, J.-L. Huang, S.-C. Hou, M.-C. Tsai, C.-C. Chang, Cu3Si enhanced crystallinity and dopamine derived nitrogen doping into carbon coated micron-sized Si/Cu3Si as anode material in lithium-ion batteries, Electrochim. Acta, 387 (2021).
[30] H. Liu, Y. Chen, Z. Wang, C. Zhang, X. Zhang, W. Zhou, J. Liu, W. Wang, P. Yu, Solid-state reaction synthesis of amorphous/nanostructured Si@SiO -Cu3Si composites by mechanical milling for lithium-ion anodes, Journal of Alloys and Compounds, 905 (2022).
[31] Y.H. Wu, O.L. Huang, S.C.E. Hou, M.C. Tsai, C.C. Chang, Cu3Si enhanced crystallinity and dopamine derived nitrogen doping into carbon coated micron-sized Si/Cu3Si as anode material in lithium-ion batteries, Electrochim. Acta, 387 (2021).
[32] S.O. Kim, A. Manthiram, A facile, low-cost synthesis of high-performance silicon-based composite anodes with high tap density for lithium-ion batteries, J. Mater. Chem. A, 3 (2015) 2399-2406.

[33] S.N.E. Zhijia Du, R. A. Dunlap,M. N. Obrovac, NixSi1-xAlloys Prepared by Mechanical Milling as NegativeElectrode Materials for Lithium Ion Batteries, J. Electrochem. Soc., 162 (2016) 6.
[34] E.G. Barbagiovanni, L.V. Goncharova, P.J. Simpson, Electronic structure study of ion-implanted Si quantum dots in a SiO2matrix: Analysis of quantum confinement theories, Physical Review B, 83 (2011).
[35] M.C.B. W.F.Banholzer, XPS, Auger study of Cu3Si and its reaction with oxygen, Surface Science, 176 (1986) 9.
[36] Y. Cao, L. Nyborg, U. Jelvestam, XPS calibration study of thin-film nickel silicides, Surface and Interface Analysis, 41 (2009) 471-483.
[37] W.F. Simanullang, H. Itahara, N. Takahashi, S. Kosaka, K.I. Shimizu, S. Furukawa, Highly active and noble-metal-alternative hydrogenation catalysts prepared by dealloying Ni-Si intermetallic compounds, Chem Commun (Camb), 55 (2019) 13999-14002.
[38] J.Y. Woo, A.Y. Kim, M.K. Kim, S.H. Lee, Y.K. Sun, G.C. Liu, J.K. Lee, Cu3Si-doped porous-silicon particles prepared by simplified chemical vapor deposition method as anode material for high-rate and long cycle lithium-ion batteries, Journal of Alloys and Compounds, 701 (2017) 425-432.
[39] J.R.D. Jing Li, An In Situ X-Ray Diffraction Study of the Reaction of Li with Crystalline Si, J. Electrochem. Soc., 154 (2007) 6.
[40] M.N. Obrovac, L.J. Krause, Reversible Cycling of Crystalline Silicon Powder, J. Electrochem. Soc., 154 (2007).
[41] M.N. Obrovac, L. Christensen, Structural changes in silicon anodes during lithium insertion/extraction, Electrochem. Solid State Lett., 7 (2004) A93-A96.
[42] Z.J. Du, H. Liu, S.N. Ellis, R.A. Dunlap, M. Zhu, M.N. Obrovac, Electrochemistry of CuxSi1-x Alloys in Li Cells, J. Electrochem. Soc., 163 (2016) A1275-A1279.
[43] Y.D. Cao, B. Scott, R.A. Dunlap, J. Wang, M.N. Obrovac, An Investigation of the Fe-Mn-Si System for Li-Ion Battery Negative Electrodes, J. Electrochem. Soc., 166 (2019) A21-A26.
[44] X. Liu, N. Bi, C. Feng, S.W. Or, Y. Sun, C. Jin, W. Li, F. Xiao, Onion-like carbon coated CuO nanocapsules: A highly reversible anode material for lithium ion batteries, Journal of Alloys and Compounds, 587 (2014) 1-5.
[45] G. Zhou, W. Ding, Y. Guan, T. Wang, C. Liu, L. Zhang, J. Yin, Y. Fu, Progress of NiO-based anodes for high-performance Li-ion batteries, Chem Rec, (2022) e202200111.
[46] R. Zhan, X. Wang, Z. Chen, Z.W. Seh, L. Wang, Y. Sun, Promises and Challenges of the Practical Implementation of Prelithiation in Lithium‐Ion Batteries, Advanced Energy Materials, 11 (2021).
[47] B. Kim, J. Ahn, Y. Oh, J. Tan, D. Lee, J.-K. Lee, J. Moon, Highly porous carbon-coated silicon nanoparticles with canyon-like surfaces as a high-performance anode material for Li-ion batteries, J. Mater. Chem. A, 6 (2018) 3028-3037.
[48] J.-H. Kim, H. Kim, H.-J. Sohn, Addition of Cu for carbon coated Si-based composites as anode materials for lithium-ion batteries, Electrochem. Commun., 7 (2005) 557-561.
[49] X.Y. Zhao, R.A. Dunlap, M.N. Obrovac, Low Surface Area Si Alloy/Ionomer Composite Anodes for Lithium-Ion Batteries, J. Electrochem. Soc., 161 (2014) A1976-A1980.

[50] R. Miao, J. Zhu, S. Kang, J. Yang, J. Wang, J. Fu, M. Li, C. Shi, In-situ mechanochemical synthesis of sub-micro Si/Sn@SiOx-C composite as high-rate anode material for lithium-ion batteries, Electrochim. Acta, 384 (2021).
[51] M. Ashuri, Q. He, L.L. Shaw, Improving cycle stability of Si anode through partially carbonized polydopamine coating, Journal of Electroanalytical Chemistry, 876 (2020).
[52] Q. Lian, Y. Lu, W. Ding, X. He, Z. Zou, C. Jiang, Si@C anode materials decorated with higher manganese silicides for enhanced rate capability and cycle stability, Applied Surface Science, 592 (2022).
[53] S. Suh, H. Yoon, H. Park, J. Kim, H.-J. Kim, Enhancing the electrochemical performance of silicon anodes for lithium-ion batteries: One-pot solid-state synthesis of Si/Cu/Cu3Si/C electrode, Applied Surface Science, 567 (2021).
[54] J. Ma, Y. Zheng, Y. Gan, J. Zhang, Y. Xia, X. He, W. Zhang, H. Huang, Improved Lithium Storage Capability of Si Anode by Ball-Milling Produced Graphitic Carbon Sheet and Fe3O4 Nanoparticles, Journal of Electronic Materials, (2022).